Impedance Control and Performance Measure of Series Elastic Actuators

Ye Zhao, *Member, IEEE*, Nicholas Paine, *Member, IEEE*, Steven Jens Jorgensen, *Student Member, IEEE*, and Luis Sentis, *Member, IEEE*

***Abstract*—Series elastic actuators (SEAs) have become prevalent in torque-controlled robots in recent years to achieve compliant interactions with environments and humans. However, designing optimal impedance controllers and characterizing impedance performance for SEAs with time delays and filtering are still underexplored problems. This article addresses the controller design problem by devising a critically damped gain design method for a class of SEA cascaded control architectures, which is composed of outer impedance and inner torque feedback loops. We indicate that the proposed gain design criterion solves optimal controller gains by maximizing phase-margin-based stability. Meanwhile, we observe a tradeoff between impedance and torque controller gains and analyze their interdependence in terms of closed-loop stability and overall impedance performance. Via the proposed controller design criterion, we adopt frequency-domain methods to thoroughly analyze the effects of time delays, filtering, and load inertia on SEA impedance performance. A novel impedance performance metric, defined as "Z-region," is proposed to simultaneously quantify achievable impedance magnitude range (i.e., Z-width) and frequency range (i.e., Z-depth). Maximizing the Z-region enables SEA-equipped robots to achieve a wide variety of Cartesian impedance tasks without alternating the control structure. Simulations and experimental implementations are performed to validate the proposed method and performance metric.**

***Index Terms*—Distributed control, impedance control, series elastic actuator (SEA), time delays, torque control.**

Manuscript received August 18, 2016; revised December 1, 2016 and May 19, 2017; accepted June 20, 2017. Date of publication August 25, 2017; date of current version December 15, 2017. This work was supported in part by the National Aeronautics and Space Administration (NASA) Johnson Space Center and the National Science Foundation (NSF), in part by the NSF/NASA NRI Grant NNX12AM03G, in part by the Office of Naval Research Grant N000141512507, and in part by the NASA Space Technology Research Fellowship Grant NNX15AQ42H. *(Corresponding author: Luis Sentis.)*

Y. Zhao was with the Department of Mechanical Engineering, The University of Texas at Austin, Austin, TX 78712 USA. He is now with the John A. Paulson School of Engineering and Applied Sciences, Harvard University, Cambridge, MA 02138 USA (e-mail: yezhao@utexas.edu).

N. Paine was with the Department of Electrical and Computer Engineering, The University of Texas at Austin, Austin, TX 78712 USA. He is now with Apptronik Systems, Inc., Austin, TX 78758 USA (e-mail: npaine@apptronik.com).

S. J. Jorgensen is with the Department of Mechanical Engineering, The University of Texas at Austin, Austin, TX 78712 USA (e-mail: stevenjj@utexas.edu).

L. Sentis is with the Department of Aerospace Engineering and Engineering Mechanics, The University of Texas at Austin, Austin, TX 78712 USA (e-mail: lsentis@austin.utexas.edu).

Color versions of one or more of the figures in this paper are available online at http://ieeexplore.ieee.org.

Digital Object Identifier 10.1109/TIE.2017.2745407

I. Introduction

SERIES elastic actuators (SEAs) [1]–[4], as an emerging actuation mechanism, provide considerable advantages in compliant and safe environmental interactions, impact absorption, energy storage, and force sensing. In the control literature, adopting cascaded impedance control architectures for SEAs has attracted increasing investigations over the last few years [3], [5], [6]. Compared to full-state feedback control [7]–[9], the cascaded control performs superior when the controlled plant comprises slow dynamics and fast dynamics simultaneously. In this case, the inner fast control loop isolates the outer slow control loop from nonlinear dynamics inherent to the physical system, such as friction and stiction. Therefore, this study focuses on the cascaded control structure to simulate the distributed control structure for humanoid robots accompanied with a variety of delayed feedback loops [10], [11]. This class of cascaded control structures nests feedback control loops [3], [5], i.e., an inner torque loop and an outer impedance loop for the task-level control, such as Cartesian impedance control. Recently, the works in [3] and [6] proposed to embed a motor velocity loop inside the torque feedback loop. This velocity feedback enables to use integral gains for counteracting static errors such as drivetrain friction, while maintaining the system's passivity. Mosadeghzad *et al.* [5] extensively studied the stability, passivity, and performance for a variety of cascaded feedback control schemes incorporating position, velocity, and torque feedback loops.

Optimal controller design methodologies are increasingly sought within the robotics and control community. Recent works in [12] devised a critically damped controller gain design criterion to accomplish high impedance for rigid actuators. However, inherent fourth-order SEA dynamics in this study make it challenging to design optimal controllers of the cascaded feedback structure. For the cascaded control, a common routine is to tune the inner loop gains first, followed by an outer loop gain tuning. Indeed, this procedure consumes substantially hand-tuning efforts and lacks optimal performance guarantees. The majority of existing results rely on empirical tuning [1], [5]. The work in [3] designed controller gain ranges according to a passivity criterion. However, gain parameters were highly coupled as a set of inequalities, which leaves the controller gains undetermined. In this paper, a fourth-order gain design criterion is proposed by simultaneously solving SEA optimal impedance gains and torque gains. The "optimality" is proposed according to phase-margin-based stability. Through this criterion, the designer only

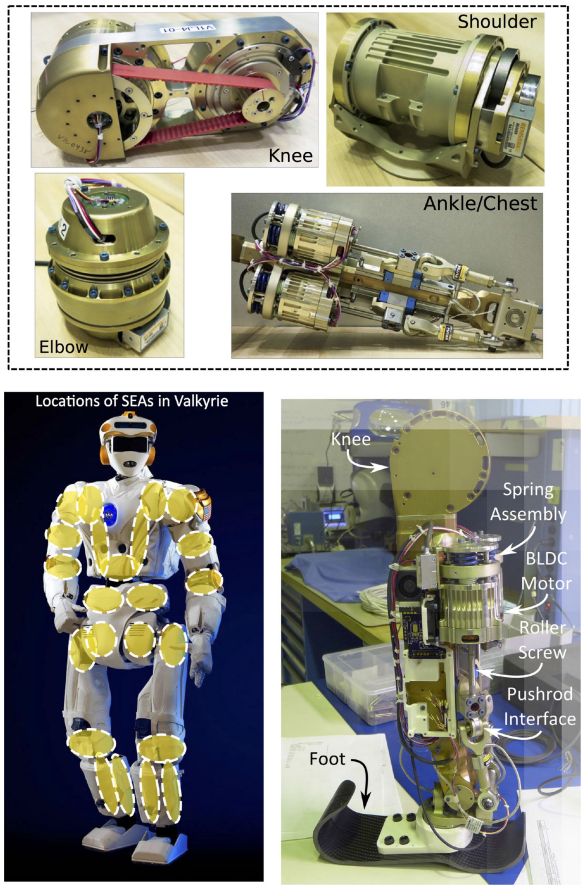

Fig. 1. Valkyrie robot equipped with SEAs. (Top) Set of high-performance NASA Valkyrie SEAs. (Bottom left) Valkyrie robot with SEA location annotations. (Bottom right) Calf and ankle structure.

needs to specify a natural frequency parameter, and then all the impedance and torque gains are deterministically solved. A larger natural frequency represents larger impedance and torque controller gains. This dimensionality reduction and automatic solving process is not only convenient for SEA controller design but also warrants optimal performance in terms of system closed-loop stability.

System passivity criteria have been extensively studied for coupled systems [7], [13], [14], networked control systems [15], and coordination control [16]. Among the robotics community, Vallery *et al.* [3] designed passivity-based controller gains for SEAs. However, that work only incorporates stiffness feedback, and the ignored damping feedback indeed plays a pivotal role, which will be analyzed in this study. Damping-type impedance control was investigated in [6]. However, it does not analyze the effects of time delays and filtering. Although these practical issues were tackled in [3], the time delays are so subtle that it cannot model large time delays often existing in serial communication channels. Due to the destabilizing effects of time delays, significant effort has been put forth to ensure that systems are stable, by enforcing passivity criteria [17]. The passivity criterion is conservative [13]. Buerger and Hogan [18] proposed a complementary stability to relax the assumptions in passivity analysis. This work claims that the system performance is merely determined by robot dynamics and unaffected by environment dynamics. However, our study reveals that the stability is indeed affected by environment (i.e., load) dynamics via frequency-domain analysis. Among various existing results, Gao *et al.* for the first time proposed an impressive and unique methodology, such that the typical network-induced imperfections including time delays, packet dropouts, and quantizations, etc., can be dealt with efficiently in a unified framework [19], [20]. This methodology is applicable to the passivity of networked control systems [15]. Overall, this line of research makes a solid foundation for the analysis and design of networked control systems, and can be further utilized to solve related remote sensing and teleoperation problems arising from industrial applications.

Real-world tasks normally necessitate a wide range of impedances. However, existing literature mainly focus on the low SEA impedance for compliant control [3], [6], [21]. This imposes a huge limitation on its capability of achieving stiff tasks. For instance, legged robots without model-based feedforward compensation require high impedance control to counteract the gravity effect. Besides the achievable impedance range, frequency characteristics of the impedance performance is frequently ignored, but it does play a vital role in large-variability impedance tasks. To fill in this gap, this study proposes the maximum achievable SEA impedance range, i.e., Z-width [22], [23] within a unified control architecture, and quantifies the achievable impedance frequency range, which is defined as "Z-depth". Our study not only confirms that SEA impedance at low frequency is constrained by the active stiffness (i.e., controller stiffness gain) while its impedance at high frequency is constrained by the passive spring stiffness, but also reveals how the impedance performance is affected by time delays and filtering.

In light of these discussions, the contributions of this paper are as follows:

1) analyzing time-domain controller stability of SEAs and proposing a critically damped gain selection criterion;
2) conducting a frequency-dependent impedance analysis of SEAs affected by time delays and filtering; and
3) devising a novel SEA impedance performance metric "Z-region," which incorporates both achievable impedance magnitude and frequency ranges.

Combining this performance metric with the controller gain selection criterion in 1) and impedance frequency analysis in 2), we achieved a unified framework of SEA impedance controller design and performance quantification, as shown in Fig. 2. We expect this study provides a promising solution of designing optimal impedance controllers for SEA-equipped humanoid robots (see Fig. 1) to achieve complex locomotion and manipulation tasks [24], [25].

II. Modeling of SEAs

This section models a SEA constituting two nested feedback loops, i.e., an outer impedance loop and an inner torque

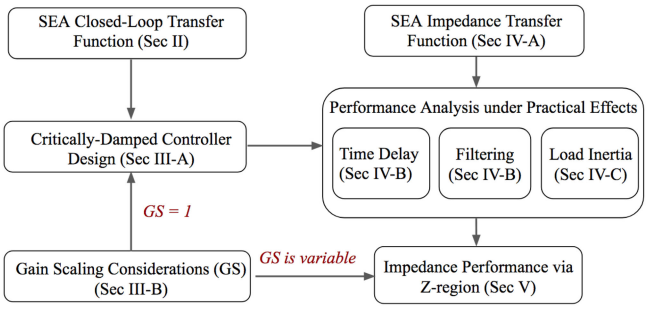

Fig. 2. Diagram depicting the roadmap for impedance control and performance analysis of SEAs. (Left) Design of practical impedance controllers, including position feedback and force feedback gains. (Right) Performance analysis under practical effects and a new criterion called the Z-region. The Z-region is a numerical measure that quantifies the achievable impedances over a frequency range.

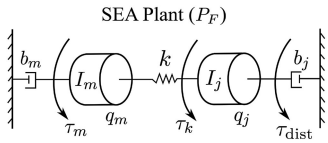

Fig. 3. SEA model. The annotated parameters are defined in Section II. We map the motor inertia I_m and motor damping b_m to the joint coordinates by multiplying by the gear reduction squared.

loop. The SEA dynamics can be modeled as shown in Fig. 3. The spring torque τ_k is

$$\tau_k = k(q_m - q_j). \tag{1}$$

where the spring stiffness is denoted by k, and q_m and q_j represent motor and joint positions, respectively. As to the joint side, it is assumed that disturbance torque $\tau_{\text{dist}} = 0$. Namely, spring torque is equal to load torque, i.e.,

$$\tau_k = I_j \ddot{q}_j + b_j \dot{q}_j. \tag{2}$$

where I_j and b_j are joint inertia and damping coefficients, respectively. Notably, this model merely models the effects of viscous friction; we leave the analysis of other types of friction for future work. Then, the load plant $P_L(s)$ has

$$P_L(s) = \frac{q_j(s)}{\tau_k(s)} = \frac{1}{I_j s^2 + b_j s}. \tag{3}$$

By (1) and (2), the following transfer function can be derived:

$$\frac{q_j(s)}{q_m(s)} = \frac{k}{I_j s^2 + b_j s + k}. \tag{4}$$

We have motor torque $\tau_m = I_m \ddot{q}_m + b_m \dot{q}_m + k(q_m - q_j)$. Combining the equation above with (4) and defining the spring deflection as $\Delta q = q_m - q_j$, we establish the following mapping from the motor angle q_m to Δq:

$$r(s) = \frac{\Delta q(s)}{q_m(s)} = \frac{I_j s^2 + b_j s}{I_j s^2 + b_j s + k}. \tag{5}$$

By (1), we can express the spring torque as

$$\tau_k(s) = k\Delta q(s) = kr(s)q_m(s). \tag{6}$$

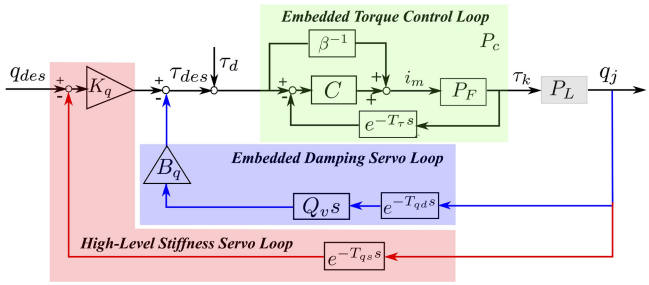

Fig. 4. SEA controller diagram. The inner torque controller is composed of a feedforward loop with a mapping scalar β^{-1} and PD torque feedback loops. The outer impedance controller constitutes stiffness and damping feedback loops. Time delays are modeled as e^{-Ts}. We apply first-order low-pass filters to both velocity and torque derivative feedback loops. τ_k represents the spring torque. The motor current input is i_m. The embedded torque control loop is denoted by P_C, which normally has faster dynamics than the outer one.

Given the relationship between the motor current i_m and the motor torque τ_m represented by $\tau_m(s)/i_m(s) = \beta = \eta N k_\tau$, with drivetrain efficiency η (constant for simplicity, and dynamic modeling of drivetrain losses is ignored), gear speed reduction[1] N and motor torque constant k_τ (see Table II in Section VI for more parameter details), the SEA plant $P_F(s)$ is represented by

$$P_F(s) = \frac{\tau_k(s)}{i_m(s)} = \frac{\beta r(s) k}{I_m s^2 + b_m s + r(s)k} \tag{7}$$

where I_m and b_m are motor inertia and damping coefficients, respectively. As shown in Fig. 4, the closed-loop torque control plant P_C is

$$P_C(s) = \frac{\tau_k(s)}{\tau_{\text{des}}(s)} = \frac{P_F(\beta^{-1} + C)}{1 + P_F C e^{-T_\tau s}}. \tag{8}$$

The torque feedback loop includes a delay term $e^{-T_\tau s}$ and a proportional-derivative (PD) compensator $C = K_\tau + B_\tau Q_{\tau d} s$ (see Fig. 4), where $Q_{\tau d}$ models a first-order low-pass filter for the torque derivative signal

$$Q_{\tau d} = \frac{2\pi f_{\tau d}}{s + 2\pi f_{\tau d}} \tag{9}$$

where $f_{\tau d}$ is the filter cutoff frequency. Additionally, a feedforward loop is incorporated to convert the desired torque τ_{des} to the motor current i_m (see Fig. 4). By (3) and (8), the following transfer function can be obtained:

$$\frac{q_j(s)}{\tau_{\text{des}}(s)} = P_L P_C = \frac{P_F(\beta^{-1} + C)}{(1 + P_F C e^{-T_\tau s})(I_j s^2 + b_j s)}. \tag{10}$$

For the impedance feedback, we have the following form:

$$\tau_{\text{des}}(s) = K_q(q_{\text{des}} - e^{-T_{qs} s} q_j) - B_q e^{-T_{qd} s} Q_{qd} s q_j \tag{11}$$

where $e^{-T_{qs} s}$ and $e^{-T_{qd} s}$ denote the time delays of stiffness and damping feedback loops, separately. The joint velocity filter Q_{qd} has the same format as that in (9) with a cutoff frequency f_{qd}. Alternatively, we can also send the desired joint velocity as

[1] N represents the ratio of motor rotary velocity to actuator linear velocity. This gear ratio is achieved by using pulley reduction N_p and ball screw, which is parameterized by ball screw lead l_{bs}. See [2] for more actuator design details.

the input of the embedded damping loop. In that case, an extra zero will show up in the numerator of (12). Since a zero only changes transient dynamics, it does not affect system stability. Using P_L and P_C in (3) and (8), we obtain the SEA closed-loop transfer function P_{CL}

$$P_{\mathrm{CL}}(s) = \frac{q_j(s)}{q_{\mathrm{des}}(s)} = \frac{K_q P_C P_L}{1 + P_C P_L (e^{-T_{qd}s} B_q Q_{qd} s + e^{-T_{qs}s} K_q)} = \frac{K_q(1 + \beta K_\tau + \beta B_\tau Q_{\tau d} s)}{\sum_{i=0}^{4} D_i s^i} \tag{12}$$

with the associated coefficients defined as

$$\begin{aligned} D_4 &= I_m I_j / k \\ D_3 &= (I_j b_m + I_m b_j)/k + I_j \beta B_\tau Q_{\tau d} e^{-T_\tau s} \\ D_2 &= I_j(1 + e^{-T_\tau s}\beta K_\tau) + I_m + b_j \beta B_\tau Q_{\tau d} e^{-T_\tau s} \\ &\quad + \beta B_\tau B_q e^{-T_{qd}s} Q_{qd} Q_{\tau d} + b_j b_m / k \\ D_1 &= b_j(1 + e^{-T_\tau s}\beta K_\tau) + b_m + \beta B_\tau Q_{\tau d} K_q e^{-T_{qs}s} \\ &\quad + e^{-T_{qd}s}(1 + \beta K_\tau) B_q Q_{qd} \\ D_0 &= e^{-T_{qs}s}(1 + \beta K_\tau) K_q. \end{aligned} \tag{13}$$

This closed-loop transfer function is sixth order due to the existence of low-pass filters Q_{qd} and $Q_{\tau d}$. Here, we formulate it in a fourth-order form for the sake of clarity. Note that, the numerator of (12) has a zero induced by the torque derivative term. As to the step response, this induced zero shortens the rise time but causes an overshoot. Nevertheless, system stability is not affected since it is solely determined by the denominator's characteristic polynomial.

III. Gain Design of SEAs

The closed-loop transfer function derived in (12) is complex due to the cascaded impedance and torque feedback loops. This complexity makes the SEA controller design challenging. In this section, we propose a critically damped criterion to design optimal controller gains.

A. Critically Damped Controller Gain Design Criterion

Impedance control gains of rigid actuators can be designed based on the well-established critically damped criterion of second-order systems [12]. As for high-order systems like SEAs, such a critically damped criterion is still missing. In this study, we aim at designing feedback controller gains such that the overall SEA closed-loop system behaves as two damped second-order systems [26]. To this end, we represent the fourth-order system in (12) (the time delays and filtering in (12) are ignored for problem tractability) by two second-order systems in multiplication presented as

$$(s^2 + 2\zeta_1\omega_1 s + \omega_1^2)(s^2 + 2\zeta_2\omega_2 s + \omega_2^2) \tag{14}$$

which has four design parameters $\omega_1, \omega_2, \zeta_1,$ and ζ_2. They will be used to design the gains K_q, B_q, K_τ, and B_τ. First, we set $\zeta_1 = \zeta_2 = 1$ in (14) to obtain the critically damped performance. Second, we assume $\omega_2 = \omega_1$ for simplicity. An optimal pole placement design is left for future work. Let us define a natural frequency f_n of (14) as

$$\omega_1 = \omega_2 \triangleq \omega_n = 2\pi f_n. \tag{15}$$

By comparing the denominators of (12) and (14), we obtain the nonlinear gain design criterion equations as

$$\begin{aligned} \frac{I_j b_m + I_m b_j + I_j \beta B_\tau k}{I_m I_j} &= 4\omega_n \\ \frac{k(I_j(1 + \beta K_\tau) + I_m + \beta B_\tau (b_j + B_q)) + b_j b_m}{I_m I_j} &= 6\omega_n^2 \\ \frac{k(b_j + B_q)(1 + \beta K_\tau) + k(b_m + \beta B_\tau K_q)}{I_m I_j} &= 4\omega_n^3 \\ \frac{(1 + \beta K_\tau) k K_q}{I_m I_j} &= \omega_n^4. \end{aligned} \tag{16}$$

These four equations with coupled gains can be solved by MATLAB's fsolve() function. Note that, representing a fourth-order system by two multiplied second-order systems in (14) maintains the properties of the fourth-order system. In our method above, the simplification comes from the selection of $\omega_1, \omega_2, \zeta_1$, and ζ_2 parameters in (14). The resulting benefit is that selecting a natural frequency uniformly determines all the gains of torque and impedance controllers. This advantage avoids the commonly adopted complicated yet heuristic controller tuning procedures, like the ones in [5], [26], although system dynamics in our case are restricted to specific patterns such as the critically damped one we design. Let us show an example as follows.

Example 1: To validate this criterion, we test five natural frequencies. We select filter cutoff frequencies $f_{vd} = 50$ Hz, $f_{\tau d} = 100$ Hz, and time delays $T_\tau = T_{qd} = 0.5$ ms, $T_{qs} = 2$ ms.[2] The solved gains and phase margins[3] are shown in Table I. Increasing f_n will lead to a uniform increase of all four gains. This property meets our expectation that increasing torque (or impedance) gains result in a torque (or impedance) bandwidth increase and a phase margin decrease.

TABLE I
CRITICALLY DAMPED CONTROLLER GAINS

Frequency (Hz)	Impedance gains (Nm/rad, Nms/rad)	Torque gains (A/Nm, As/N m)	Phase margin
$f_n = 12$	$K_q = 65$ $B_q = 0.46$	$K_\tau = 1.18$ $B_\tau = 0.057$	45.1°
$f_n = 14$	$K_q = 83$ $B_q = 0.76$	$K_\tau = 1.80$ $B_\tau = 0.067$	43.2°
$f_n = 16$	$K_q = 103$ $B_q = 1.02$	$K_\tau = 2.56$ $B_\tau = 0.077$	40.0°
$f_n = 18$	$K_q = 124$ $B_q = 1.26$	$K_\tau = 3.45$ $B_\tau = 0.087$	36.5°
$f_n = 20$	$K_q = 148$ $B_q = 1.49$	$K_\tau = 4.48$ $B_\tau = 0.097$	33.2°

[2]These filters and delays are only used in the phase-space computation based on (12) and ignored in the critically damped selection criterion for problem tractability.

[3]It is worth noting that the phase margin is computed based on the open-loop transfer function derived from P_{CL} in (12).

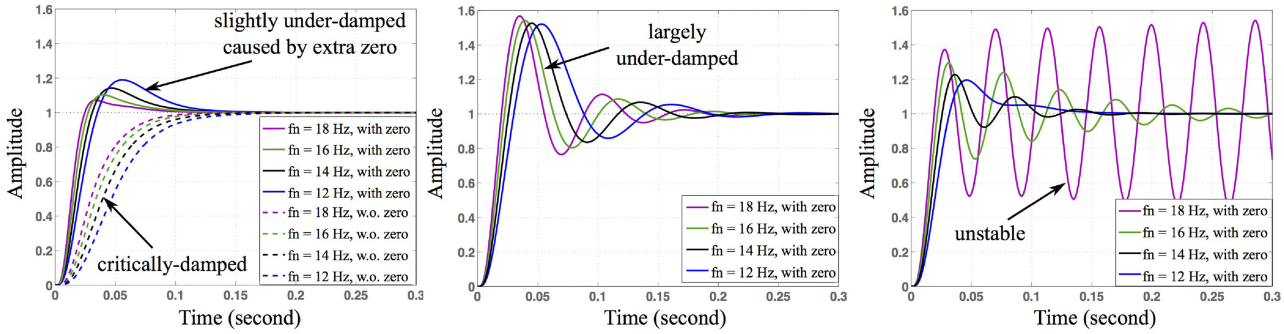

(a) $T_\tau = T_{qs} = T_{qd} = 0.5$ ms (b) $T_\tau = T_{qd} = 0.5$ ms, $T_{qs} = 8$ ms (c) $T_\tau = T_{qs} = 0.5$ ms, $T_{qd} = 8$ ms

Fig. 5. SEA step response affected by time delays. These subfigures demonstrate that the larger delays that impedance feedback loops have, the worse performance that the step response has. (b) and (c) SEA stability has a higher sensitivity to damping delays than the stiffness counterpart. In (a), it is revealed that larger f_n leads to a larger overshoot, which appears to be counterintuitive. However, by close inspection, we can observe that the largest f_n in solid magenta already shows distortion, and its 36.4° phase margin is the smallest among all four cases. To study the influence of zero in (12), step responses without this zero are also simulated and represented by dashed lines in (a). By comparison, we can realize an overshoot induced by this extra zero.

Note that, for simplicity, the gain design above ignores time delay, which does affect system stability. Next, we will study the effect of time delays given this gain design criterion. Since torque feedback is the inner loop, it normally suffers a smaller delay than that in the outer impedance loop. That is why we assign $T_\tau = 0.5$ ms in the example above. Notice that T_{qs} is chosen to be larger than T_{qd} since the former belongs to the outer control loop whereas the latter belongs to the inner control loop. The benefits of having damping feedback in the inner loop were extensively analyzed in [12]. Also, we show how time delays affect SEA step response in Fig. 5. This motivates us to implement the impedance feedback loops in a distributed pattern as shown in Fig. 4. Namely, we allocate the stiffness feedback loop at the high level while embedding the damping feedback loop at the low level for a fast servo rate. The same distributed control strategy was implemented for the rigid actuators in [12] and extended lately for the whole-body operational space control [27].

B. Tradeoff Between Torque and Impedance Control

During gain tuning of the SEA-equipped bipedal robot Hume [28] and NASA Valkyrie robot, which have similar SEA control architectures as the one in Fig. 4, a pivotal phenomenon is observed: If one increases torque controller gains or decreases impedance controller gains, the robot tends to become unstable. To reason about this observation, we propose a SEA gain scale definition as follows.

Definition 1 (SEA Gain Scale): The gain scale of a SEA's cascaded controller is a scaling parameter GS between adjusted gains (K_{i_a}, B_{i_a}) and nominal gains (K_{i_n}, B_{i_n}), $i \in \{\tau, q\}$

$$\text{GS} = \frac{K_{\tau_a}}{K_{\tau_n}} = \frac{K_{q_n}}{K_{q_a}}, \quad \text{GS} = \frac{B_{\tau_a}}{B_{\tau_n}} = \frac{B_{q_n}}{B_{q_a}} \tag{17}$$

where the adjusted gains denote actual gains in use while the nominal gains denote reference ones designed by the critically damped gain design criterion.

It should be noted that if GS $= 1$, then the adjusted gains are the same as the nominal gains. For example, the controller gains in Table I are five sets of nominal gains. By (17), we have the following equalities:

$$K_{\tau_a} \cdot K_{q_a} = K_{\tau_n} \cdot K_{q_n}, \quad B_{\tau_a} \cdot B_{q_a} = B_{\tau_n} \cdot B_{q_n} \tag{18}$$

which maintain the same multiplicative value of nested proportional (or derivative) torque and impedance gains for the normal and adjusted conditions. An overall controller gain design procedure is shown in Algorithm 1.

Algorithm 1: Gain Controller Design Procedure.

Assign system parameters *sysParam* in (12).
Assign natural frequency f_n (i.e., ω_1 and ω_2 by (15)),
$\zeta_1 = \zeta_2 \leftarrow 1$.
procedure CONTROLLERSOLVER (f_n, ζ_1, ζ_2, *sysParam*)
  Deterministically solve nominal controller gains K_{q_n}, $B_{q_n}, K_{\tau_n}, B_{\tau_n}$ ▷ refer to (16)
  if Gain scale GS $= 1$ **then**
    $(K_q, B_q, K_\tau, B_\tau) \leftarrow (K_{q_n}, B_{q_n}, K_{\tau_n}, B_{\tau_n})$
  else
    $(K_{q_a}, B_{q_a}) \leftarrow (K_{q_n}, B_{q_n})$/GS
    $(K_{\tau_a}, B_{\tau_a}) \leftarrow$ GS $\cdot (K_{\tau_n}, B_{\tau_n})$ ▷ refer to (17)
    $(K_q, B_q, K_\tau, B_\tau) \leftarrow (K_{q_a}, B_{q_a}, K_{\tau_a}, B_{\tau_a})$
  end if
  return $(K_q, B_q, K_\tau, B_\tau)$
end procedure
Assign filtering parameters $f_{vd}, f_{\tau d}$ and time delays T_τ, T_{qs}, T_{qd}.
PM $=$ PhaseMargin
$(K_q, B_q, K_\tau, B_\tau, f_{vd}, f_{\tau d}, T_\tau, T_{qs}, T_{qd})$

There is a tradeoff between a large torque bandwidth for accurate torque tracking and a low torque bandwidth for larger achievable impedance range. The work in [14] obtained a similar observation that enlarging the inner loop controller bandwidth reduces the range of stable impedance control gains. In their experimental validations, they do not decrease impedance gains when raising torque gains. As it is known, the product of cascaded gains grows if torque gains increase; however, this

TABLE II
UT-SEA PARAMETERS

Parameter	Value	Parameter	Value	Parameter	Value
Spring stiffness k	350 000N/m	Joint pulley radius r_k	0.025 m	Motor inertia I_m	0.225 kg $\cdot$m^2
Joint inertia I_j	0.014 kg $\cdot$m^2	Motor damping b_m	1.375 N$\cdot$ms/rad	Joint damping b_j	0.1 N$\cdot$ms/rad
Gear reduction N	8.3776×10^3	Ball screw lead l_{bs}	0.003 m/rev	Drivetrain efficiency η	0.9
Motor torque coeff. k_τ	0.0276 N$\cdot$m/A	Pulley reduction N_p	4	Sample rate	1 kHz

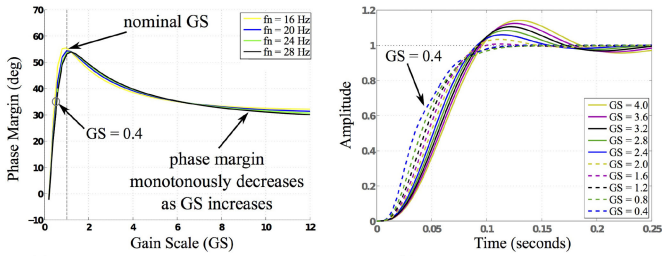

(a) Phase margin with varying GS and fn (b) Step response with varying GS

Fig. 6. Optimality of the critically damped gain design criterion. (a) Samples a variety of gain scales and natural frequencies. An optimal performance is achieved by using the proposed critically damped gain design criterion. (b) Larger overshoot but slow rise time when GS $>$ 1 and an over-damped response with distortions when GS $<$ 1.

increase is not considered in their stability analysis. It is therefore unclear if the reduced stable impedance range is caused by enlarging the torque gains or the increased product gain due to the coupled effect of torque and impedance gains. To validate the tradeoff in a more realistic manner, our method maintains a constant gain product value as shown in (18). Fig. 6(a) shows the sampling results for different gain scales GS. A larger GS indicates increased torque gains with decreased impedance gains. When GS $>$ 1, an increasing GS deteriorates the system stability (i.e., phase margin) and causes a larger oscillatory step response as shown in Fig. 6(b). On the other hand, when GS $<$ 1, a decreasing G also decreases the system stability. For instance, GS $= 0.4$ corresponds to a 34° phase margin, as shown in (a), and accordingly, a distortion appears in the step response of (b). We ignore delays and filtering to focus on the effects of the gain scale. The tests in Fig. 6 validate the optimal performance (i.e., maximized phase margin) of our proposed critically damped gain design criterion (i.e., GS $= 1$). Although GS $= 1$ is the optimal value for stability, changing GS to different values allows us to change the impedance behavior, i.e., the "Z-region" in Section V, without changing the natural frequency. Thus, we assign GS as a design parameter in Algorithm 1. In Section IV, we will analyze the frequency-domain SEA impedance.

IV. SEA Impedance Analysis

Impedance control is widely used for dynamic interaction between a robot and its physically interacting environment [29]. In this section, we study SEA impedance performance in the frequency domain. In particular, we first derive the SEA impedance transfer function given the SEA controller diagram in Fig. 4, and then analyze the effects of time delays, filtering, and load inertia.

A. SEA Impedance Transfer Function

The SEA impedance transfer function is defined with a joint velocity $\dot{q}_j$ input and a joint torque τ_j output. Based on zero desired joint position q_{des}, the SEA impedance $Z(s) = \tau_j(s)/(-sq_j(s))$ is formulated as follows:

$$Z(s) = \frac{\tau_j(s)}{-sq_j(s)} = \frac{\sum_{i=0}^{4} N_{zi} s^i}{\sum_{i=0}^{5} D_{zi} s^i} \tag{19}$$

with the numerator coefficients

$$\begin{aligned}
N_{z4} &= I_m T_{f\tau} T_{fv} \beta k \\
N_{z3} &= \beta k (I_m (T_{f\tau} + T_{fv}) + T_{f\tau} T_{fv} b_m) \\
N_{z2} &= I_m \beta k + \beta k b_m (T_{f\tau} + T_{fv}) + k k_\tau \\
&\quad (T_{f\tau} + \beta(B_\tau + K_\tau T_{f\tau}))(B_q e^{-T_{qd} s} + K_q T_{fv} e^{-T_{qs} s}) \\
N_{z1} &= b_m \beta k + B_q k k_\tau (1 + K_\tau \beta) e^{-T_{qd} s} + K_q k k_\tau \\
&\quad (T_{fv} + T_{f\tau} + \beta(B_\tau + K_\tau (T_{f\tau} + T_{fv})))e^{-T_{qs} s} \\
N_{z0} &= K_q k k_\tau e^{-T_{qs} s} (1 + K_\tau \beta)
\end{aligned}$$

and the denominator coefficients

$$\begin{aligned}
D_{z5} &= I_m T_{f\tau} T_{fv} \beta, D_{z4} = I_m \beta (T_{fv} + T_{f\tau}) + T_{fv} T_{f\tau} \beta b_m \\
D_{z3} &= \beta I_m + \beta b_m (T_{f\tau} + T_{fv}) + T_{fv} k \beta (T_{f\tau} \\
&\quad + k_\tau (B_\tau + K_\tau T_{f\tau}) e^{-T_\tau s}) \\
D_{z2} &= \beta (b_m + T_{f\tau} k + k k_\tau (B_\tau + K_\tau T_{f\tau}) e^{-T_\tau s}) \\
&\quad + T_{fv} \beta k (1 + K_\tau k_\tau e^{-T_\tau s}) \\
D_{z1} &= \beta k (1 + K_\tau k_\tau e^{-T_\tau s}), D_{z0} = 0.
\end{aligned}$$

Note that, $Z(s)$ in (19) does not incorporate the joint inertia I_j and damping b_j since these parameters belong to parts of the interacting environment. Equation (19) explicitly models time delays and filtering, which are often ignored in the literature of SEA cascaded controller architectures with PD-type controllers. Also, the SEA transfer function in (19) is complete without any approximations.

B. Effects of Time Delays and Filtering

The SEA impedance frequency responses are demonstrated in Fig. 7. We analyze various scenarios either with or without time delays and filtering.

i) $Z_i(j\omega)$ is the ideal impedance without delays and filtering.
ii) $Z_f(j\omega)$ is the impedance only with filtering.

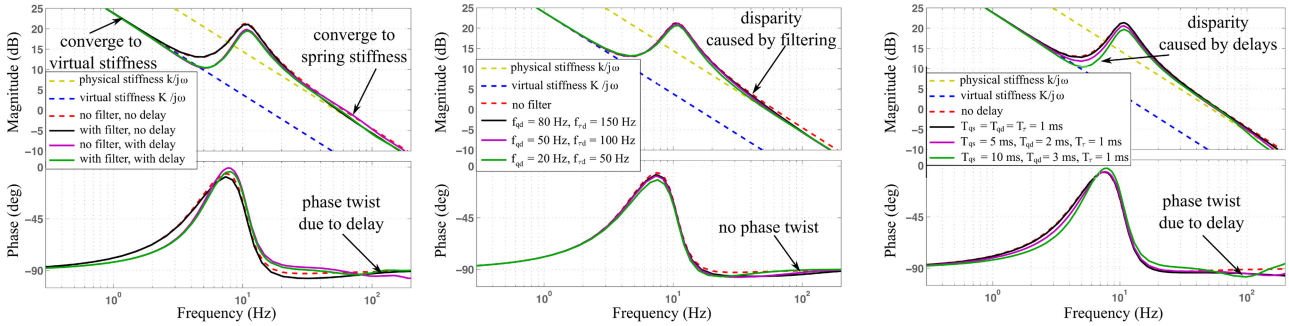

(a) SEA impedance with/w.o filter and delay (b) SEA impedance only with filter (c) SEA impedance only with feedback delays

Fig. 7. SEA impedance with time delays and filtering. (a) Impedance of a physical spring $k/(j\omega)$ and a virtual stiffness gain controller are shown by yellow and blue dashed lines, respectively. The ideal SEA impedance without delay and filtering is represented by a red dashed line. At low frequency range, SEA impedance converges to the virtual stiffness. A similar behavior was observed in [3]. At high frequency range, it approaches another impedance asymptote. (b) Analysis of the filtering effect. (c) Analysis of the time delay effect. Accordingly, the sensitivity discrepancy of different time delays can be analyzed but is not discussed here due to the space limitations. These simulations have a natural frequency $f_n = 30$ Hz, corresponding to $K_q = 293.6$ N·m/rad, $B_q = 2.49$ N · m·s/rad, $K_\tau = 11.71$ A/N·m, and $B_\tau = 0.146$ As/N·m.

iii) $Z_d(j\omega)$ is the impedance only with delays.

iv) $Z_{fd}(j\omega)$ is the impedance with both delays and filtering.

At low frequency range, the SEA impedance converges to a virtual stiffness asymptote in all scenarios (when time delays are considered, we have $e^{-T_{qs}\,j\omega} \to 1, e^{-T_\tau\,j\omega} \to 1$ as $\omega \to 0$)

$$\lim_{\omega\to 0} Z_c(j\omega) = \lim_{\omega\to 0} \frac{N_{z0}}{j\omega \cdot D_{z1}} = \frac{K_q k_\tau(\beta^{-1} + K_\tau)}{j\omega \cdot (1 + K_\tau k_\tau)}$$

where $c \in \{i, f, d, fd\}$. The denominator of the final expression has a $j\omega$ term, which indicates a -20 dB/dec decay rate. The low-frequency impedance $Z_c(j\omega)$ behaves as a constant stiffness impedance $K_q/j\omega$ scaled by a constant $k_\tau(\beta^{-1} + K_\tau)/(1 + K_\tau k_\tau)$. This scaling applies to any PD-type cascaded impedance controller. Note that, $k_\tau \beta^{-1}$ is normally a small value. When $k_\tau K_\tau$ is large enough, $Z_c(j\omega)$ approaches $K_q/(j\omega)$, i.e., a pure virtual spring. This meets our intuition.

As to the high frequency range, the impedance also approaches an asymptote with a potential twist, depending on the delay and filtering conditions. First, let us start with the ideal case (i), i.e., without delays and filtering. This leads to $D_{z5} = D_{z4} = 0$, and we have

$$\lim_{\omega\to+\infty} Z_i(j\omega) = \lim_{\omega\to+\infty} \frac{N_{z2}}{j\omega \cdot D_{z3}} = \frac{k(I_m + k_\tau B_\tau B_q)}{j\omega \cdot I_m}$$

which represents a constant stiffness-type impedance scaled from the passive spring stiffness $k/(j\omega)$. The red dashed lines in Fig. 7 illustrate this ideal SEA impedance feature.

Second, we derive case (iii) only with delay, that is, $T_{fv} = T_{f\tau} = 0$. Then, $D_{z5} = D_{z4} = 0$, and we obtain

$$\lim_{\omega\to+\infty} Z_d(j\omega) = \lim_{\omega\to+\infty} \frac{N_{z2}}{j\omega \cdot D_{z3}} = \frac{k(I_m + k_\tau B_\tau B_q e^{-T_{qd}\,s})}{j\omega \cdot I_m}.$$

Since the complex number $e^{-T_{qd}\,s}$ rotates along the unit circle, the SEA impedance will periodically twist around the passive spring stiffness at high frequency range. This is visualizable in Fig. 7(c).

Third, in case (ii) only with filtering, we have $T_{qs} = T_{qd} = T_\tau = 0$ and then obtain

$$\lim_{\omega\to+\infty} Z_f(j\omega) = \frac{N_{z4}}{j\omega D_{z5}} = \frac{k}{j\omega}$$

which represents a passive spring stiffness as shown in Fig. 7(b). The curve does not twist thanks to the constant limit value $k/(j\omega)$. To verify the applicability of the aforementioned behaviors to different natural frequencies, we analyze the SEA impedance performance under varying natural frequencies in Fig. 8. By comparing Fig. 8(a) and (b) [or Fig. 7(b) and (c)], we conclude that time delays have a larger effect on the SEA impedance than filtering.

C. Effect of Load Inertia

This section analyzes the effect of load inertia on SEA impedance performance. A second-order model of the output load $I_j s + b_j$ is added to (19), i.e., $Z_l(j\omega) = Z(j\omega) + I_j s + b_j$. Since (19) becomes $Z(j\omega) \to 0$ as $\omega \to +\infty$, we have

$$\lim_{\omega\to+\infty} Z_l(j\omega) = \lim_{\omega\to+\infty} (Z(j\omega) + I_j \cdot j\omega + b_j) = I_j \cdot j\omega + b_j$$

where $I_j \cdot j\omega$ represents a 20-dB/dec asymptote at high frequencies (see Fig. 9); the damping term b_j adds a constant offset. As the equation above shows, at high frequency range, SEA impedance behaves as a spring-mass impedance instead of a pure spring one. In particular, this impedance is dominated by the load inertia as shown in Fig. 9. This figure simulates three scenarios with different load inertias. Different than the load mass effect studied in [3], our study has a large focus on analyzing the effect of filtering and time delays. These two factors dominate at middle frequency range where large spikes show up in the shaded region of Fig. 9. The larger load inertia is, the smaller spike the response has.

V. SEA Impedance Characterization

In this section, we propose a novel metric to characterize SEA impedance performance in terms of both achievable

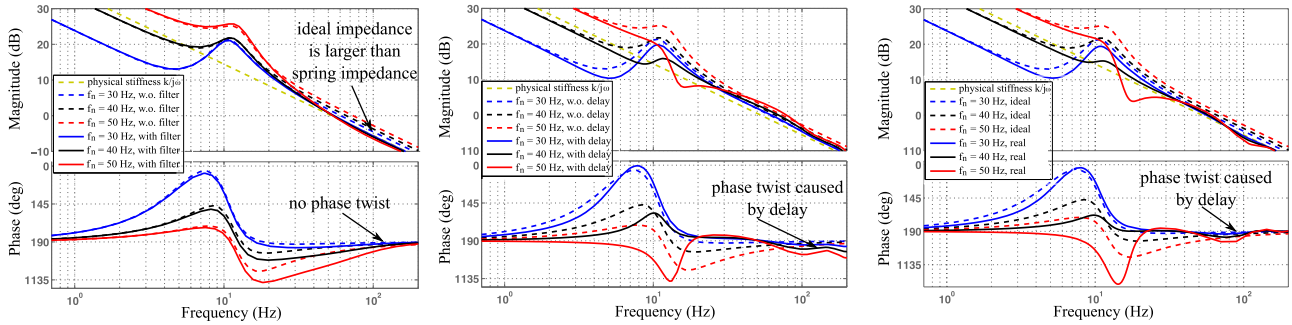

(a) SEA impedance with varying fn with/w.o. filter, no delay

(b) SEA impedance with varying fn with/w.o. delay, no filter

(c) SEA impedance with varying fn with/w.o. delay and filter

Fig. 8. SEA impedance with varying natural frequencies f_n. First, these subfigures validate that a higher natural frequency f_n results in higher SEA impedance. (a) and (b) show how time delay and filtering affect SEA impedance, respectively. We use filters with $f_{qd} = 50$ Hz and $f_{\tau d} = 100$ Hz, whereas time delays are chosen as $T_{qd} = T_\tau = 1$ ms, $T_{qs} = 10$ ms. Second, we test the cases with both filters and delays, as shown in (c), and compare them with ideal cases with neither filter nor delays.

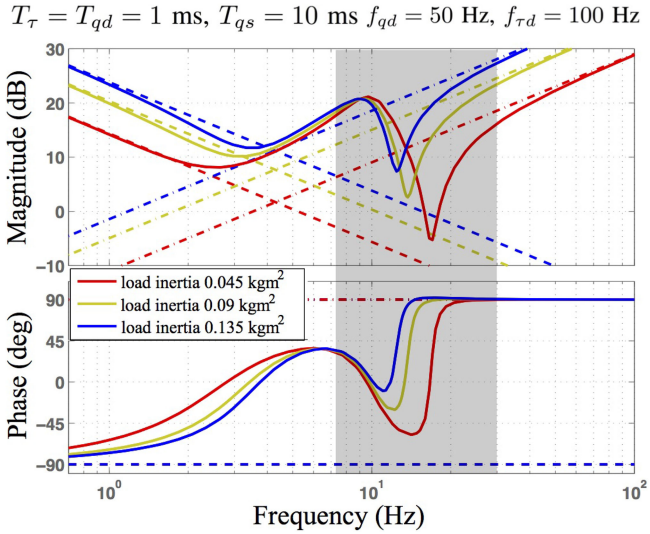

Fig. 9. SEA impedance with varying load inertias. Three different load scenarios are illustrated. All of them use the natural frequency $f_n = 20$ Hz, corresponding to $K_q = 148$ N·m/rad, $B_q = 1.49$ N · m·s/rad, $K_\tau = 4.48$ A/N·m, and $B_\tau = 0.097$ As/N·m. The damping term is $b_j = 0.1$ N · m·s/rad. For all three scenarios, dashed lines are used to represent asymptote at low and high frequencies, respectively. Since the load inertia is modeled, the SEA impedance approaches the load inertia impedance curve $I_j \cdot j\omega + b_j$ at high frequencies.

magnitude and frequency ranges. The controller gains are designed by using the critically damped gain design criterion and the gain scale defined in Definition 1. The Z-width proposed in the haptics community [22], [30] only characterizes the achievable impedance magnitude range. In the recent work of [31], a new concept, "M-width" was proposed to quantify the passive range of a pure virtual mass in the frequency domain. However, characterizing the achievable impedance range in the frequency domain is yet an open problem. To quantify the achievable frequency range, we define a new concept: the "Z-depth". A frequency range within which the achievable impedance magnitude range is nonzero (i.e., nonzero Z-width). Given the Z-width and Z-depth concepts, we propose the following definition of "Z-region."

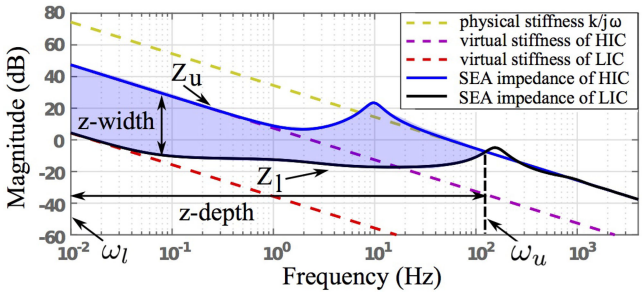

Fig. 10. Z-region surrounded by the highest impedance controller (HIC) and the lowest impedance controller (LIC). This figure shows achievable SEA impedance ranges by modulating the gain scale GS, as defined in Definition 1. The control gains are solved using the critically damped gain design criterion.

Definition 2 (Z-region): A frequency-domain region composed of the achievable impedance magnitude range (Z-width) over a particular frequency range (Z-depth)

$$Z_{\text{region}} = \int_{\omega_l}^{\omega_u} W(\omega)\Big|\log|Z_u(j\omega)| - \log|Z_l(j\omega)|\Big| d\omega \quad (20)$$

where ω_l and ω_u are lower and upper boundaries of achievable frequencies, respectively. Z_u and Z_l are the upper and lower boundaries of the achievable impedances, respectively, as shown in Fig. 10 . $W(\omega)$ is a weighting value function depending on frequency ω.

Equation (20) uses a log scale. ω_u is determined via the intersection of Z_u and Z_l impedance lines whereas ω_l is a sufficiently small frequency and normally chosen by the designer. In theory, any infinitely small positive frequency will appear into the Z-depth. However, in practice values of ω_l are usually within $[10^{-3}, 10^{-1}]$ Hz, depending on specific system specifications. The weighting function $W(\omega)$ can be used to emphasize a specific frequency range. To give an intuition of the Z-region we describe the following example.

Example 2: First, we choose $W(\omega) = 1$ to treat all frequencies equal. The natural frequency is chosen as $f_n = 15$ Hz. Filters have $f_{vd} = 50$ Hz, $f_{\tau d} = 100$ Hz, and time delays are chosen with $T_\tau = T_{qd} = 1$ ms and $T_{qs} = 10$ ms. Given these

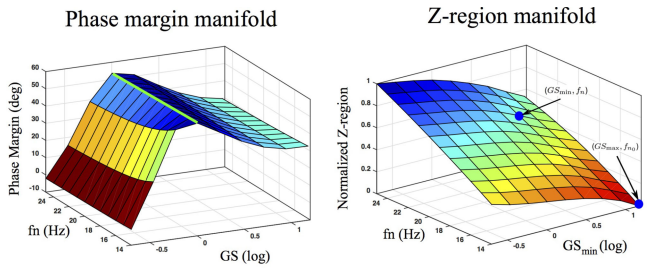

Fig. 11. Stability and impedance performance maps. The phase margin manifold and Z-region manifold represent the system stability and impedance performance, respectively. The gain scale GS is expressed in logarithmic scale. The searching range is GS $\in [0.2, 15]$. Note that, GS axis in the right figure represents the minimal GS, i.e., $\mathrm{GS}_{\min}$. We sample a set of equidistant $\mathrm{GS}_{\min}$ values while fixing $\mathrm{GS}_{\max} = 15$. The normalized Z-region is numerically computed based on the boundary impedance lines defined by the varying $(\mathrm{GS}_{\min}, f_n)$ pair and a constant pair $(\mathrm{GS}_{\max}, f_{n_0})$, where $f_{n_0} = 14$ Hz. The natural frequency range is $f_n \in [14, 25]$ Hz.

parameters, we search for the minimum gain scale $\mathrm{GS}_{\min}$ such that the HIC remains stable. We heuristically set $\mathrm{GS}_{\min} = 0.1$. As shown in Fig. 6, when GS > 1 and GS increases, the phase margin approaches a positive constant value. Thus, we manually set the maximum gain scale $\mathrm{GS}_{\max}$ as 10^3. As shown in Fig. 10, the Z-region is represented by the blue shaded region, surrounded by HIC and LIC impedance lines (corresponding to $\mathrm{GS}_{\max}$ and $\mathrm{GS}_{\min}$, respectively). The Z-depth is bounded in the frequency range by $(\omega_l, \omega_u) = (10^{-2}, 120)$ Hz. In this case, ω_l is empirically chosen and ω_u is selected by the intersection of HIC and LIC lines. In fact, at $100-200$ Hz, the LIC impedance boundary line has a small resonant peak that is induced by the time delays and filtering. We ignore this resonant peak for simplicity.

Given the phase margin analysis in Section III and the proposed Z_{region} metric, let us generate SEA stability and impedance performance maps. The phase margin manifold and the Z-region manifold, as shown in Fig. 11, are sampled with respect to various natural frequencies f_n and gain scales GS. The Z_{region} is normalized to the values within $[0, 1]$. The gain scale GS uses a logarithmic scale for visualization convenience. As shown in Fig. 11(a), the maximum phase margin represented by the peak green line is always achieved at around GS $= 1$ (i.e., 0 in the log scale) for all sampled natural frequencies f_n. This further validates the optimality of our critically damped gain design criterion. Fig. 11(b) shows the effects of natural frequencies and gain scales on the Z-region.

VI. Experimental Validation

This experiment section validates the proposed methods and criterion on our SEA testbed, parameters of which are provided in Table II. We employ the gain design criterion proposed in Section III to design controller gains. Detailed stiffness and damping gains are accessible in Table I. All of our tests have a 1-kHz sampling rate, which induces 0.5-ms effective feedback delay. To obtain larger feedback delays, a software buffering of sampling data is manually implemented. Thus, the total

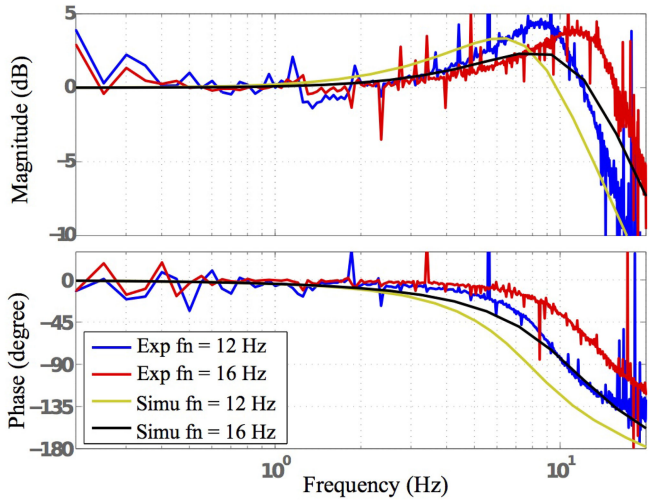

Fig. 12. Impedance frequency responses with different f_n. At low frequencies, experimental results are matched with the simulations. Compared to simulations, the experimental data shows a larger peak at the resonant frequency and a slightly larger bandwidth. The parameters are $T_{qs} = T_{qd} = T_\tau = 0.5$ ms, $f_{qd} = 50$ Hz, $f_{\tau d} = 100$ Hz, and GS $= 1$.

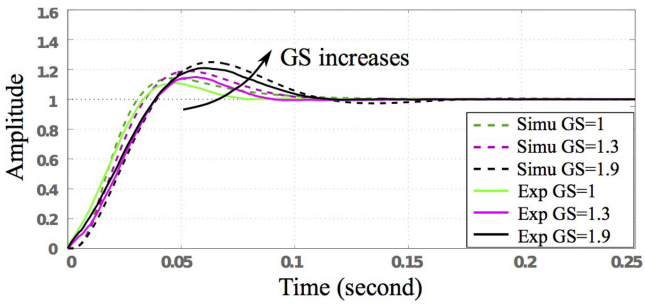

Fig. 13. Step responses with different gain scales. The overshoot in the experimental results, when GS is increased, matches our simulation predictions. The parameters are $T_{qs} = T_{qd} = T_\tau = 1$ ms, $f_{qd} = 50$ Hz, $f_{\tau d} = 100$ Hz, and $f_n = 14$ Hz.

feedback delay has two components

$$T_d = \frac{T_s}{2} + T_e \tag{21}$$

where T_s is the sampling period and T_e is the extra added feedback delay. T_s is divided by 2 since the effective delay is half of the sampling period [32]. The extra feedback delay T_e represents large round-trip communication delay between low-level and high-level architectures. The source code is public online.[4] We also provide a video link of experimental validations.[5]

In Fig. 12, a larger natural frequency produces a higher closed-loop bandwidth. Simulations match experimental results except slight discrepancies at high frequencies. To validate the trade-off between impedance gains and torque gains, we test step responses as shown in Fig. 13. The result shows that when GS > 1, a larger GS slows down the rise time and produces a larger overshoot. This observation is consistent with our theoretical

[4]https://github.com/YeZhao/series-elastic-actuation-impedance-control
[5]https://youtu.be/biIdlcAMPyE

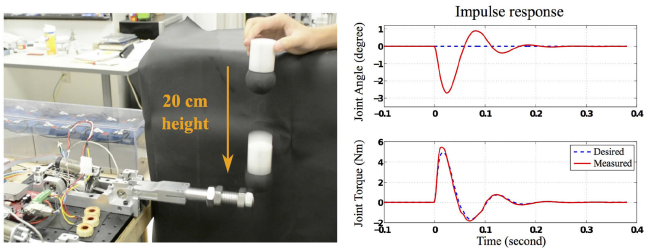

Fig. 14. Impulse response of UT-SEA. A ball is dropped from a constant height (20 cm) and exerts an impulse force on the arm end-effector. The maximum angle deviation is around 2.5°. The arm recovers to its initial position within 0.3 s. Joint torque tracking is accurate.

analysis that SEA phase margin will be reduced by decreasing impedance gains and increasing torque gains. As for the discrepancy between simulations and experiments, a potential reason is due to the different spring location in the simulation model and the hardware. The simulation model assumes the spring to be placed between the gearbox output and the load (a.k.a., force sensing SEA), whereas our UT-SEA hardware places the spring between the motor housing and the chassis ground (a.k.a., reaction force sensing SEA) for compact size design. This discrepancy affects impedance characteristics only at the resonant frequency and high-frequency, which is also validated by the result in Fig. 12. The reason why we choose a force sensing SEA model is due to being more general in the SEA literature, it is more suitable for force control, and simplicity in the force measurements. For more details regarding these two mechanical designs, see [2]. The discrepancy between the two models is negligible in our tests since our primary target is to validate the tradeoff between impedance and torque control.

Torque tracking under impact dynamics is important for interactive manipulation and bipedal locomotion. By implementing an impulse test, we show the high-fidelity of our torque control under external impulse disturbances. The purpose of this test is to validate the performance of the controller under disturbances. The controller gains correspond to those of $f_n = 14$ Hz in Table I. As shown in Fig. 14, when a ball free falls from a 20-cm height and hits the arm with an impulse force, the SEA actuator settles down promptly and recovers after approximately 0.3 s. The recovery to the disturbance is fast and the tracking performance of the torque controller is very accurate.

VII. Discussions and Conclusion

The main focus of this study was to address the problem of impedance controller design and performance characterization of SEAs by incorporating time delays and filtering over a wide frequency spectrum. In particular, we proposed a critically damped controller gain selection method of the cascaded SEA control structure. By uncovering the tradeoff existing between impedance gains and torque gains, we proved the optimality of our gain design criterion. More importantly, we have proposed a new concept dubbed "Z-region" to quantify the SEA impedance performance. Compared with the Z-width metric, the proposed "Z-region" quantifies both the impedance magnitude and frequency range in a unified metric. Based on this metric, we numerically estimated the Z-region and analyzed how the natural frequency and gain scaling affect this impedance region. We believe the critically damped gain selection criterion and the Z-region metric can be applied to many types of SEAs and robotics systems for performance analysis and optimizations.

Acknowledgment

The authors would like to thank the members of the Human Centered Robotics Laboratory, The University of Texas at Austin, for their great help and support.

References

[1] G. A. Pratt, P. Willisson, C. Bolton, and A. Hofman, "Late motor processing in low-impedance robots: Impedance control of series-elastic actuators," in *Proc. Amer. Control Conf.*, 2004, pp. 3245–3251.
[2] N. Paine, S. Oh, and L. Sentis, "Design and control considerations for high-performance series elastic actuators," *IEEE/ASME Trans. Mechatronics*, vol. 19, no. 3, pp. 1080–1091, 2014.
[3] H. Vallery, J. Veneman, E. van Asseldonk, R. Ekkelenkamp, M. Buss, and H. van Der Kooij, "Compliant actuation of rehabilitation robots," *IEEE Robot. Autom. Mag.*, vol. 15, no. 3, pp. 60–69, Sep. 2008.
[4] J. Lu, K. Haninger, W. Chen, and M. Tomizuka, "Design and torque-mode control of a cable-driven rotary series elastic actuator for subject–robot interaction," in *Proc. IEEE Int. Conf. Adv. Intell. Mechatronics*, 2015, pp. 158–164.
[5] M. Mosadeghzad, G. A. Medrano-Cerda, J. A. Saglia, N. G. Tsagarakis, and D. G. Caldwell, "Comparison of various active impedance control approaches, modeling, implementation, passivity, stability and trade-offs," in *Proc. IEEE/ASME Int. Conf. Adv. Intell. Mechatronics*, 2012, pp. 342–348.
[6] N. L. Tagliamonte, D. Accoto, and E. Guglielmelli, "Rendering viscoelasticity with series elastic actuators using cascade control," in *Proc. IEEE-RAS Int. Conf. Robot. Autom.*, 2014, pp. 2424–2429.
[7] A. Albu-Schäffer, C. Ott, and G. Hirzinger, "A unified passivity-based control framework for position, torque and impedance control of flexible joint robots," *Int. J. Robot. Res.*, vol. 26, no. 1, pp. 23–39, 2007.
[8] M. Hutter, C. D. Remy, M. A. Hoepflinger, and R. Siegwart, "Efficient and versatile locomotion with highly compliant legs," *IEEE/ASME Trans. Mechatronics*, vol. 18, no. 2, pp. 449–458, Apr. 2013.
[9] A. De Luca, B. Siciliano, and L. Zollo, "PD control with on-line gravity compensation for robots with elastic joints: Theory and experiments," *Automatica*, vol. 41, no. 10, pp. 1809–1819, 2005.
[10] C.-L. Fok, G. Johnson, J. D. Yamokoski, A. Mok, and L. Sentis, "Controlit!—A software framework for whole-body operational space control," *Int. J. Human. Robot.*, vol. 13, no. 1, 2016.
[11] Y. Sakagami, R. Watanabe, C. Aoyama, S. Matsunaga, N. Higaki, and K. Fujimura, "The intelligent ASIMO: System overview and integration," in *Proc. IEEE/RSJ Int. Conf. Intell. Robots Syst.*, vol. 3, 2002, pp. 2478–2483.
[12] Y. Zhao, N. Paine, K. S. Kim, and L. Sentis, "Stability and performance limits of latency-prone distributed feedback controllers," *IEEE Trans. Ind. Electron.*, vol. 62, no. 11, pp. 7151–7162, Nov. 2015.
[13] T. Hulin, C. Preusche, and G. Hirzinger, "Stability boundary for haptic rendering: Influence of physical damping," in *Proc. IEEE/RSJ Int. Conf. Intell. Robots Syst.*, 2006, pp. 1570–1575.
[14] M. Focchi *et al.*,"Robot impedance control and passivity analysis with inner torque and velocity feedback loops," *Control Theory Technol.*, vol. 14, no. 2, pp. 97–112, 2016.
[15] H. Gao, T. Chen, and T. Chai, "Passivity and passification for networked control systems," *SIAM J. Control Optim.*, vol. 46, no. 4, pp. 1299–1322, 2007.
[16] S. Yin, H. Yang, and O. Kaynak, "Coordination task triggered formation control algorithm for multiple marine vessels," *IEEE Trans. Ind. Electron.*, vol. 64, no. 6, pp. 4984–4993, Jun. 2017.
[17] J. E. Colgate and G. Schenkel, "Passivity of a class of sampled-data systems: Application to haptic interfaces," in *Proc. Amer. Control Conf.*, vol. 3, 1994, pp. 3236–3240.
[18] S. P. Buerger and N. Hogan, "Complementary stability and loop shaping for improved human–robot interaction," *IEEE Trans. Robot.*, vol. 23, no. 2, pp. 232–244, Apr. 2007.

[19] H. Gao, T. Chen, and J. Lam, "A new delay system approach to network-based control," *Automatica*, vol. 44, no. 1, pp. 39–52, 2008.
[20] H. Gao and T. Chen, "H_∞ estimation for uncertain systems with limited communication capacity," *IEEE Trans. Autom. Control*, vol. 52, no. 11, pp. 2070–2084, Nov. 2007.
[21] K. Kong, J. Bae, and M. Tomizuka, "Control of rotary series elastic actuator for ideal force-mode actuation in human–robot interaction applications," *IEEE/ASME Trans. Mechatronics*, vol. 14, no. 1, pp. 105–118, 2009.
[22] J. E. Colgate and J. M. Brown, "Factors affecting the z-width of a haptic display," in *Proc. IEEE-RAS Int. Conf. Robot. Autom.*, 1994, pp. 3205–3210.
[23] T. Boaventura, G. A. Medrano-Cerda, C. Semini, J. Buchli, and D. G. Caldwell, "Stability and performance of the compliance controller of the quadruped robot HyQ," in *Proc. IEEE/RSJ Int. Conf. Intell. Robots Syst.*, 2013, pp. 1458–1464.
[24] S. Kuindersma *et al.*,"Optimization-based locomotion planning, estimation, and control design for the atlas humanoid robot," *Auton. Robots*, vol. 40, no. 3, pp. 429–455, 2016.
[25] H. Dai, A. Valenzuela, and R. Tedrake, "Whole-body motion planning with centroidal dynamics and full kinematics," in *Proc. IEEE-RAS Int. Conf. Human. Robots*, 2014, pp. 295–302.
[26] F. Petit and A. Albu-Schaffer, "State feedback damping control for a multi DOF variable stiffness robot arm," in *Proc. IEEE-RAS Int. Conf. Robot. Autom.*, 2011, pp. 5561–5567.
[27] Y. Zhao and L. Sentis, "Passivity of time-delayed whole-body operational space control with series elastic actuation," in *Proc. IEEE-RAS Int. Conf. Human. Robots*, 2016, pp. 1290–1297.
[28] D. Kim, Y. Zhao, G. Thomas, B. R. Fernandez, and L. Sentis, "Stabilizing series-elastic point-foot bipeds using whole-body operational space control," *IEEE Trans. Robot.*, vol. 32, no. 6, pp. 1362–1379, 2016.
[29] N. Hogan, "Impedance control: An approach to manipulation: Part II implementation," *J. Dyn. Syst., Meas. Control*, vol. 107, no. 1, pp. 8–16, 1985.
[30] J. S. Mehling, J. E. Colgate, and M. A. Peshkin, "Increasing the impedance range of a haptic display by adding electrical damping," in *Proc. Eurohaptics Conf. Symp. Haptic Interfaces Virtual Environ. Teleoperator Syst.*, 2005, pp. 257–262.
[31] N. Colonnese and A. M. Okamura, "M-width: Stability, noise characterization, and accuracy of rendering virtual mass," *Int. J. Robot. Res.*, vol. 34, no. 6, pp. 781–798, 2015.
[32] T. Hulin, C. Preusche, and G. Hirzinger, "Stability boundary for haptic rendering: Influence of human operator," in *Proc. IEEE/RSJ Int. Conf. Intell. Robots Syst.*, 2008, pp. 3483–3488.

Ye Zhao (S'10–M'16) received the B.E. degree in control science and engineering from Harbin Institute of Technology, Harbin, China, in 2011 and the M.S. and Ph.D. degrees in mechanical engineering from The University of Texas at Austin, Austin, TX, USA, in 2013 and 2016, respectively, where he also received the UT Robotics Graduate Portfolio Program degree in 2016.

He is currently a Postdoctoral Fellow with the John A. Paulson School of Engineering and Applied Sciences, Harvard University, Cambridge, MA, USA. His research interests include robust motion planning and optimization, high-level task planning, whole body operational space control, distributed impedance control of series elastic actuators, and legged robotic systems.

Dr. Zhao was a Co-Chair of the IEEE Robotics and Automation Society (RAS) Student Activities Committee and a Committee Member of IEEE-RAS Member Activities Board. He is also an ICT Chair of the 2018 IEEE/RSJ International Conference on Intelligent Robots and Systems, an Associate Editor of the 2017 IEEE-RAS International Conference on Humanoid Robots, an Associate Editor of the 2017 IEEE Workshop on Advanced Robotics and its Social Impact, and a Review Editor of Frontiers in Robotics and AI: Humanoid Robotics.

Nicholas Paine (S'12–M'16) received the B.S., M.S., and Ph.D. degrees from The University of Texas at Austin,, Austin, TX, USA, in 2008, 2010, and 2014, respectively, all in electrical engineering.

In 2015, he was a Postdoctoral Researcher in the Human Centered Robotics Lab. He is currently the Chief Technology Officer at Apptronik Systems, Inc., Austin, TX, USA. His research interests include design and control of actuators and systems for dynamic legged robots.

Dr. Paine received the Virginia and Ernest Cockrell, Jr. Fellowship in engineering in 2008.

Steven Jens Jorgensen (S'17) received the B.S. Engineering degree from the Mechanical Engineering Department, Massachusetts Institute of Technology, Cambridge, MA, USA, and the M.S. Engineering degree from the Mechanical Engineering Department, The University of Texas at Austin, Austin, TX, USA, in 2014 and 2017, respectively.

In 2015, he received the NASA Space Technology Research Fellowship (NSTRF), which supported his graduate studies for four years. Under the NSTRF, he is with the NASA Johnson Space Center and helps deploy human–robot interaction algorithms on Valkyrie: NASA's humanoid robot. His research interests include human-aware whole-body control, motion planning, activity and intent recognition, and productive human–robot interaction.

Luis Sentis (S'04–M'07) received the Ph.D. degree in electrical engineering from Stanford University, Stanford, CA, USA.

He is currently an Associate Professor of aerospace engineering and engineering mechanics at the University of Texas at Austin (UTA), Austin, TX, USA, and the co-founder of Apptronik Systems Inc., Austin. He was a La Caixa Foundation Fellow. He worked in Silicon Valley in the high-tech sector leading Research and Development projects in clean room automation. At UTA, he leads the Human Centered Robotics Laboratory: an experimental facility focusing on control and embodiment of humanoid robots. His research interests include realtime control of human-centered robots, design of high performance humanoid robots, and safety protocols in robotics.

Prof. Sentis received the NASA Elite Team Award for his contributions to NASA's Johnson Space Center Software Robotics and Simulation Division.